Enhanced vibrational electron energy-loss spectroscopy of adsorbate molecules

David Kordahl* and Christian Dwyer†
Department of Physics, Arizona State University, Tempe, Arizona 85287, USA

(Received 10 December 2018; published 28 March 2019)

Plasmonic excitations in metallic nanoparticles are known to depend strongly on nanoparticle size and shape. Here we explore how such excitations can be harnessed to enhance the vibrational signals from molecules adsorbed on nanoparticle surfaces, as detected using electron energy-loss spectroscopy in the scanning transmission electron microscope. We use the Born-Huang formalism in the electrostatic approximation to develop a theoretical model for electron energy-loss from an adsorbed molecule (represented by a point dipole) on the surface of a dielectric nanoparticle. We find that the adsorbate contribution to the energy-loss spectrum is approximately proportional to the square of the electric field at the adsorption site, and hence we find that the enhancement of the molecule's vibrational signal is greatest for molecules adsorbed on small, sharp nanoparticles. When the molecular frequency is near one of the nanoparticle frequencies, we generally find an asymmetric Fano-type spectrum line shape whose asymmetry is attributable to multimodal contributions. Our calculations for a molecule adsorbed on the tip of a prolate spheroidal silver nanoparticle predict that signal enhancements of several hundred times should be readily achievable, and up to several thousand times if the nanoparticle's plasmonic mode is "tuned" to the molecular frequency. Such enhancement effects potentially make vibrational STEM-EELS a powerful tool for the characterization of surface-functionalized nanoparticles and nanomaterials used for chemical sensing.

DOI: 10.1103/PhysRevB.99.104110

I. INTRODUCTION

It has become possible in recent years to use high-energy electrons in a scanning transmission electron microscope (STEM) to perform electron energy-loss spectroscopy (EELS) on the vibrational properties of materials [1–6]. One advantage of this form of vibrational spectroscopy is that it encourages the study of freestanding nanomaterials, whereas Raman and infrared spectroscopies typically require materials to be either in bulk form or residing on a thick substrate. Another advantage is that the STEM's intrinsically high spatial resolution permits nanometer spatial resolution in vibrational spectroscopy [4], which in turn should allow for the vibrational study of local inhomogeneities [7–9]. Aloof-beam measurements of vibrational properties also make it possible to achieve a spatial resolution of tens of nanometers without causing radiation damage to the sample [1,5].

Recent experiments [10,11] have confirmed the adequacy of the dielectric description for quantitative prediction of optical-vibrational EELS signals, and recent numerical work on vibrational inelastic scattering [12] has shown the dielectric description to be useful for incorporating long-wavelength modes into detailed simulations. The size and shape of the sample have important implications for the long-wavelength modes. These effects are characterized by the sample's shape on a scale of hundreds of nanometers and are caused by the macroscopic electric fields associated with nontransverse optical-vibrational excitations. Studies of optical-vibrational modes of dielectric materials with various canonical shapes form an extensive literature that spans several decades [13–20].

The primary purpose of this paper is to explore how nanoparticle shape effects might be harnessed to enhance the vibrational EELS signals from molecules adsorbed at the surface of a nanoparticle. The analogy here is with tip-enhanced Raman spectroscopy, where large signal enhancements can be achieved by bringing a sharp metallic tip near the sample [21]. In that case, as in the EELS case, the molecular surroundings enhance the local electric field relative to the electric field from the probe, and the signal enhancement can be related to the electric field enhancement at the molecular adsorption site [22].

To translate this effect, we develop a classical model for EELS signals in the STEM from an adsorbed molecule (represented by a point dipole) coupled to the plasmonic excitations of a metallic nanoparticle. For a molecular frequency well separated from the plasmonic frequencies, the model predicts weaker enhancement with a symmetric spectral line shape, whereas for a resonance condition we obtain stronger enhancement which can exhibit a Fano-type asymmetric line shape due to multimodal contributions. We find that the molecular signal enhancement is approximately proportional to the square of the electric field at the adsorption site, and hence that the enhancement is greatest for a molecule adsorbed on a small nanoparticle with a highly curved surface. Our results are in good agreement with the recent work of Konečná *et al.* [23] who used the dielectric formalism to describe the STEM-EELS of a thin molecular layer on metallic nanoparticles. We predict enhancement factors of several hundred times using silver nanoparticles with

*david.kordahl@asu.edu
†christian.dwyer@asu.edu

moderate aspect ratios, and enhancements of several thousand times by tuning the aspect ratio to a resonance condition. Such enhancement directly increases the sensitivity of molecular vibrational STEM-EELS, and it could provide a powerful tool for characterizing surface-functionalized nanoparticles and nanomaterials used for chemical sensing.

This paper is organized as follows. We begin by summarizing the established classical theory of vibrational properties for dielectric solids in the electrostatic approximation (Sec. II). We then present our theoretical treatment which solves for the case of a molecule adsorbed on the surface of a dielectric nanoparticle and the corresponding EEL spectra (Sec. III). To expound the effects of nanoparticle size and shape, we carry out explicit calculations of EEL spectra for thin foils, long cylinders, spheres, and various oblate/prolate spheroids (Sec. IV). Detailed calculations of enhancement of adsorbed molecular signals for prolate spheroids are presented and discussed (Sec. V) before concluding.

II. HARMONIC MODES IN THE BORN-HUANG THEORY

The phenomenological model of Born and Huang [24,25] treats the dielectric response of an ionic material in the continuum approximation. Here we apply the model to particles with surfaces. We also use the electrostatic approximation, which neglects magnetic effects and tends to introduce a $\sim$10% blueshift in the calculated vibrational frequencies [26].

The Born-Huang equations read

$$\begin{aligned} \ddot{\mathbf{u}} &= -\omega_0^2\mathbf{u} - 2\eta\dot{\mathbf{u}} + Z_0^*\mathbf{E}^{\text{in}}, \\ \mathbf{P} &= Z_0^*\mathbf{u} + \frac{\epsilon_\infty - 1}{4\pi}\mathbf{E}^{\text{in}}, \end{aligned} \tag{1}$$

where $\mathbf{u}$ is the displacement of ions from their equilibrium positions multiplied by $(\mu/\Omega)^{1/2}$, and where μ is the reduced mass and Ω is the volume of the ionic pair. Here $\mathbf{E}^{\text{in}}$ is the macroscopic electric field inside the nanoparticle, and $\mathbf{P}$ is the polarization density. The Born-Huang equations are manifestly local. The first treats the ionic displacement at a given position inside the nanoparticle as a damped harmonic oscillator driven by the macroscopic electric field. The second stipulates that displacements give rise to a polarization density, even as fast-moving charges captured by ϵ_∞ provide electronic screening.

The model includes four physical parameters: the transverse resonant frequency ω_0, the effective ionic charge Z_0^*, the high-frequency dielectric constant ϵ_∞, and a damping parameter η. The effective charge Z_0^* is a measure of the longitudinal optical-transverse optical splitting (where ω_ℓ is the bulk longitudinal frequency), or, equivalently, of the split between the low- and high-frequency limits of the dielectric function (ϵ_0 and ϵ_∞, respectively):

$$4\pi(Z_0^*)^2 = \epsilon_\infty\left(\omega_\ell^2 - \omega_0^2\right) = (\epsilon_0 - \epsilon_\infty)\omega_0^2. \tag{2}$$

The Born-Huang Eqs. (1) are supplemented with the equation of electrostatics:

$$\nabla\cdot\mathbf{D} = \nabla\cdot\epsilon\mathbf{E} = \nabla\cdot(\mathbf{E} + 4\pi\mathbf{P}) = 0. \tag{3}$$

This requires no free charges to be present and that the normal component of the electric displacement and the tangential component of the electric field are continuous across the nanoparticle's surface. We suppose that $\mathbf{u}$, $\mathbf{P}$, and $\mathbf{E}$ are all continuous, smooth functions inside the nanoparticle, having time dependence $\exp(-i\omega t)$, which gives us the Born-Huang dielectric function $\epsilon(\omega)$:

$$\epsilon(\omega) = \epsilon_\infty\frac{\omega(\omega + 2i\eta) - \omega_\ell^2}{\omega(\omega + 2i\eta) - \omega_0^2}. \tag{4}$$

The ω of $\epsilon(\omega)$ is complex as a result of the η term in the equations of motion, which causes the oscillatory motion to be damped. For all vibrational modes, the time variation is $\exp(-\eta t)\exp(-i(\omega_u^2 - \eta^2)^{1/2}t)$, where ω_u is the undamped vibrational frequency (e.g., $\omega_u = \omega_0$ for transverse modes, and $\omega_u = \omega_\ell$ for longitudinal modes). Hence damping causes a slight redshift.

A. Harmonic modes (surface modes)

Helmholtz-Hodge decomposition [27] allows any displacement $\mathbf{u}$ to be written as the sum of unique transverse, longitudinal, and harmonic components:

$$\mathbf{u} = \mathbf{u}_t + \mathbf{u}_\ell + \mathbf{u}_h, \quad \begin{aligned} \nabla\cdot\mathbf{u}_t &= 0, & \nabla\times\mathbf{u}_t &\neq 0, \\ \nabla\cdot\mathbf{u}_\ell &\neq 0, & \nabla\times\mathbf{u}_\ell &= 0, \\ \nabla\cdot\mathbf{u}_h &= 0, & \nabla\times\mathbf{u}_h &= 0. \end{aligned} \tag{5}$$

The harmonic components $\mathbf{u}_h$ are only present in nanoparticles with surfaces. We can similarly decompose $\mathbf{P}$ and $\mathbf{E}$. In the electrostatic approximation $\mathbf{E}_t = 0$, and so there can be no electron scattering from the transverse modes in the electrostatic approximation. Since both $\mathbf{E}_\ell$ and $\mathbf{E}_h$ can be nonzero, both longitudinal and harmonic modes can give rise to EELS signals. We expect longitudinal modes to dominate for large, thick samples, and harmonic modes to dominate for small, thin samples.

In this paper, we will consider nanoparticles up to thicknesses of 50 nm, and so we restrict our attention to the harmonic modes $\mathbf{u}_h$ (also called "surface modes," as their polarization charge $-\nabla\cdot\mathbf{P}_h$ must vanish everywhere except the nanoparticle surface). The harmonic displacements inside the nanoparticle can be put in terms of the scalar harmonic potentials:

$$\mathbf{u}_h^{\text{in}} = \nabla\phi_h^{\text{in}}, \quad \nabla^2\phi_h^{\text{in}} = 0. \tag{6}$$

By analogy, we introduce the notation that

$$\mathbf{u}_h^{\text{out}} = \nabla\phi_h^{\text{out}}, \quad \nabla^2\phi_h^{\text{out}} = 0. \tag{7}$$

For simple geometries, we can use the well-known solid harmonic solutions to Laplace's equation as our scalar potentials ϕ_h. We have scaled ϕ_h^{in} and ϕ_h^{out} such that ϕ_h is continuous at the nanoparticle surface for each mode h. We list the coordinate systems and their associated harmonic functions in the Appendix.

If $\hat{\mathbf{n}}$ is the unit normal vector at the nanoparticle surface, we can find the value ϵ_h that the dielectric function must take on to fulfill the electrostatic boundary conditions for a given harmonic mode h:

$$\epsilon_h = \left.\frac{\mathbf{u}_h^{\text{out}}\cdot\hat{\mathbf{n}}}{\mathbf{u}_h^{\text{in}}\cdot\hat{\mathbf{n}}}\right|_{\text{surface}}. \tag{8}$$

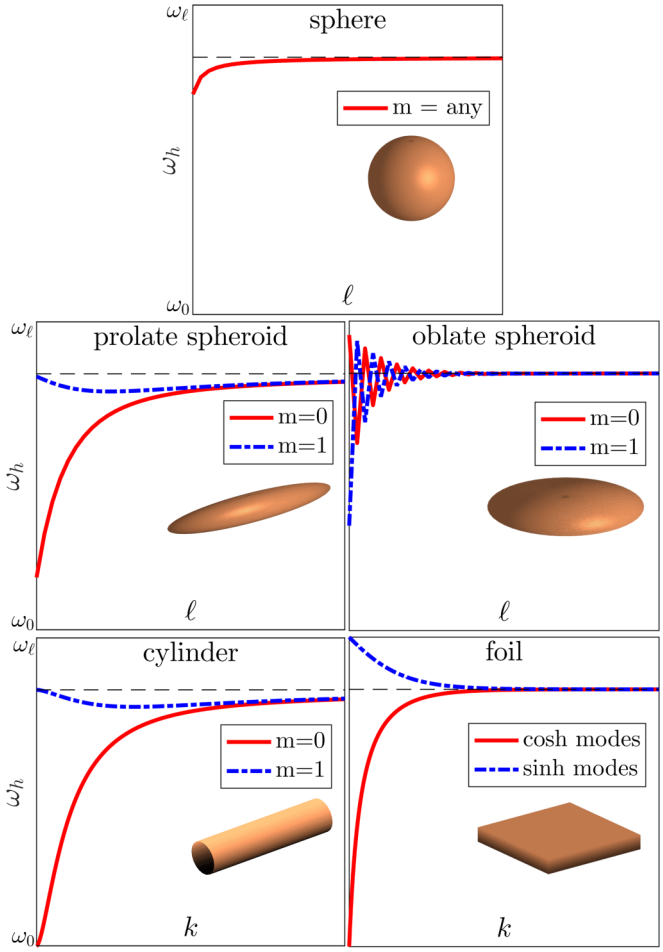

FIG. 1. Comparison of harmonic frequencies across five canonical geometries. The dashed horizontal line is at the value of ω_h for which $\epsilon_h = -1$. Sphere and spheroid plots display frequencies for $\ell = 1$–40, with the spheroids having cross-sectional eccentricites of 0.99. Cylinder and foil plots display frequencies for $k \approx 0$–$0.2\,\mathrm{nm}^{-1}$ for particles having maximal midpoint thicknesses of 50 nm.

Notice that ϵ_h is negative for these harmonic solutions. In the undamped limit, the harmonic electric field both inside and outside the nanoparticle is

$$\mathbf{E}_h = -\frac{4\pi Z_0^*}{\epsilon_\infty - \epsilon_h}\mathbf{u}_h, \tag{9}$$

and the harmonic frequencies $\epsilon(\omega_h) = \epsilon_h$ are

$$\omega_h^2 = \frac{\epsilon_\infty \omega_\ell^2 - \epsilon_h \omega_0^2}{\epsilon_\infty - \epsilon_h}. \tag{10}$$

In Fig. 1, we plot the harmonic mode frequencies for five particle geometries, for the mode labels given in Table II of the Appendix. Although nanoparticle shape restricts the range of available values for ϵ_h (and hence for ω_h), we can easily identify the transverse and longitudinal limits:

$$\begin{aligned} -\epsilon_h &\to \infty, \quad \omega_h \to \omega_0, \\ -\epsilon_h &\to 0, \quad \omega_h \to \omega_\ell. \end{aligned} \tag{11}$$

We can also note that, for each geometry, as $h \to \infty$ the harmonic frequency approaches the value for which $\epsilon_h = -1$.

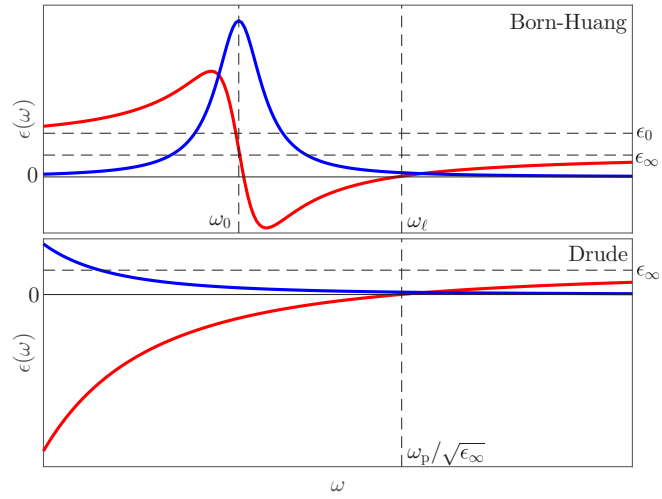

FIG. 2. Dielectric functions for the Born-Huang and Drude models, with real (red) and imaginary (blue) parts. In the Born-Huang model, a vanishing real part specifies the longitudinal frequency ω_ℓ, while in the Drude model it specifies the bulk plasma frequency ω_p.

This reflects the fact that large values of h correspond to rapid spatial variations in the surface charge. Since the high-order multipoles are short ranged, this convergence in frequency corresponds to local oscillations that are effectively decoupled.

B. Surface vibrations vs surface plasmons

As has been long been recognized [28,29], the Born-Huang model is formally equivalent to the Drude model for metals in the case where the oscillators have no restoring force, and with limits taken as follows:

$$\omega_0 \to 0, \quad Z_0^* \sqrt{4\pi} \to \omega_\mathrm{p}. \tag{12}$$

This allows plasmons to function as longitudial optical phonons in the long-wavelength limit, and implies that many of the results for bulk and surface plasmons will translate to the vibrational context. The Born-Huang and Drude dielectric functions are compared in Fig. 2.

C. Generalization to irregular geometries

As a final comment in this section, we emphasize that these methods are not limited to the "separable" nanoparticle geometries considered in this paper. The methods can be extended to irregularly shaped nanoparticles, as long as their surfaces remain smooth. It can be shown that the harmonic potential obeys the eigenvalue equation,

$$\phi_h^\mathrm{in}(\mathbf{r}) = \frac{\epsilon_h^{-1} - 1}{4\pi} \int_S d\mathbf{S} \cdot \frac{\mathbf{r} - \mathbf{r}'}{|\mathbf{r} - \mathbf{r}'|^3} \phi_h(\mathbf{r}'), \tag{13}$$

where ϵ_h now acts as an eigenvalue. One could scan the parameter space for values of ϵ_h that support solutions to Laplace's equation for an irregular shape, and the largest negative value of ϵ_h would then align with the lowest-energy mode. Eq. (13) is equivalent to computational treatments of

surface plasmons that introduce a mesh to find the electrostatic normal modes of the surface charge density [26,30].

III. DIELECTRIC NANOPARTICLE WITH A SURFACE MOLECULE

In this section, we obtain concise expressions for the expected STEM-EELS signal from an aloof electron passing a point dipole near the surface of a dielectric nanoparticle. The dipole here is meant to model an adsorbed molecule, and the nanoparticle surface is defined by a single coordinate ξ_1 in an orthogonal separable coordinate system—e.g., in spherical, oblate spheroidal, or prolate spheroidal coordinates.

The calculation begins with an expansion of the Coulomb potential in terms of the harmonic functions ϕ_h discussed above [31]. For two points $\mathbf{r}_<$ and $\mathbf{r}_>$ with radial components $\xi_{1<} < \xi_{1>}$, the Coulomb potential can be written as

$$\frac{1}{|\mathbf{r}_> - \mathbf{r}_<|} = \sum_h C_h \phi_h^{\text{in}}(\mathbf{r}_<)\bar{\phi}_h^{\text{out}}(\mathbf{r}_>). \tag{14}$$

where the C_h are real coefficients, and the overbar notation, here and following, denotes a complex conjugate. Each ϕ_h is separable into a real-valued "radial" part and a complex-valued "surface" part,

$$\begin{aligned}\phi_h^{\text{in}} &= R_h^{\text{in}}(\xi_1)S_h(\xi_2,\xi_3),\\ \phi_h^{\text{out}} &= R_h^{\text{out}}(\xi_1)S_h(\xi_2,\xi_3),\end{aligned} \tag{15}$$

where ϕ_h can be made continuous across the particle surface by requiring that $R_h^{\text{in}}(\xi_1^0) = R_h^{\text{out}}(\xi_1^0)$, where ξ_1^0 is the particular value of the ξ_1 coordinate defining the nanoparticle boundary. Then the coefficients C_h can calculated as

$$C_h = 4\pi\left(W\left(R_h^{\text{out}}, R_h^{\text{in}}\right)\int_S dS\,\frac{\bar{S}_h S_h}{h_1}\right)^{-1}, \tag{16}$$

where W is the Wronskian, the integral is over the nanoparticle's surface ξ_1^0, and h_1 is the scale factor of the radial coordinate. The Appendix gives these factors explicitly for our regular geometries, and shows how C_h can be found for the general case.

A. Applying boundary conditions

The potential due to the beam electron can be expanded using C_h. If the beam electron follows a straight path along the optic axis with $z = vt$ and transverse coordinate $\mathbf{x}$, we can write its potential near the origin in terms of harmonic functions:

$$\Phi_{\text{e}}(\mathbf{r}, t) = \sum_h -eC_h\phi_h^{\text{in}}(\mathbf{r})\bar{\phi}_h^{\text{out}}(\mathbf{x}, vt). \tag{17}$$

Taking the Fourier transform, this becomes

$$\Phi_{\text{e}}(\mathbf{r}, \omega) = \sum_h -eC_h\phi_h^{\text{in}}(\mathbf{r})I_h(\mathbf{x}, \omega), \tag{18}$$

with $I_h(\mathbf{x}, \omega)$ being the projection integral of the harmonic potential defined by

$$I_h(\mathbf{x}, \omega) = \int_{-\infty}^{\infty}\frac{dz}{v}\,\bar{\phi}_h^{\text{out}}(\mathbf{x}, z)\,e^{i\omega z/v}. \tag{19}$$

And if we suppose that the dipole $\mathbf{p}$ (the molecule) points along the nanoparticle surface normal such that

$$\mathbf{p}(\omega) = p(\omega)\hat{\mathbf{n}}, \tag{20}$$

then the dipole potential

$$\Phi_{\text{m}}(\mathbf{r}, \omega) = \mathbf{p}(\omega)\cdot\nabla_{\text{m}}\frac{1}{|\mathbf{r} - \mathbf{r}_{\text{m}}|} \tag{21}$$

can also be expanded using C_h:

$$\begin{aligned}\Phi_{\text{m}}^{\text{in}}(\mathbf{r}, \omega) &= \sum_h C_h p(\omega)\hat{\mathbf{n}}\cdot\bar{\mathbf{u}}_h^{\text{out}}(\mathbf{r}_{\text{m}})\phi_h^{\text{in}}(\mathbf{r}),\\ \Phi_{\text{m}}^{\text{out}}(\mathbf{r}, \omega) &= \sum_h C_h p(\omega)\hat{\mathbf{n}}\cdot\bar{\mathbf{u}}_h^{\text{in}}(\mathbf{r}_{\text{m}})\phi_h^{\text{out}}(\mathbf{r}).\end{aligned} \tag{22}$$

Using these expressions, we write the electric potential outside and inside the dielectric nanoparticle in terms of unknown coefficients $A_h(\omega)$ and $B_h(\omega)$:

$$\begin{aligned}\Phi_{\text{out}}(\mathbf{r}, \omega) &= \Phi_{\text{e}}(\mathbf{r}, \omega) + \Phi_{\text{m}}^{\text{in/out}}(\mathbf{r}, \omega) + \sum_h A_h(\omega)\phi_h^{\text{out}}(\mathbf{r}),\\ \Phi_{\text{in}}(\mathbf{r}, \omega) &= \sum_h B_h(\omega)\phi_h^{\text{in}}(\mathbf{r}).\end{aligned} \tag{23}$$

Notice that in applying the electrostatic boundary conditions we use $\Phi_{\text{m}}^{\text{in}}(\mathbf{r}, \omega)$ for the molecular contribution to $\Phi_{\text{out}}(\mathbf{r}, \omega)$ since the dipole is positioned strictly on the outside of the nanoparticle's surface. Applying the boundary conditions, we find that

$$A_h(\omega) = C_h\alpha_h(\omega)\left[eI_h(\mathbf{x}, \omega) - p(\omega)\hat{\mathbf{n}}\cdot\bar{\mathbf{u}}_h^{\text{out}}(\mathbf{r}_{\text{m}})\right], \tag{24}$$

where, following Ferrell *et al.* [32] and using ϵ_h as defined in Eq. (8) above, we have introduced the nanoparticle polarizability:

$$\alpha_h(\omega) = \frac{\epsilon(\omega) - 1}{\epsilon(\omega) - \epsilon_h}. \tag{25}$$

B. The molecular dipole

We suppose the molecular dipole $p(\omega)$ has a charge q, reduced mass μ, damping factor γ, and bare resonant frequency ω_{m}. If the dipole is driven by the electric field $\mathbf{E}(\omega)$ along $\hat{\mathbf{n}}$, its equation of motion,

$$\frac{q^2}{\mu}\hat{\mathbf{n}}\cdot\mathbf{E}(\omega) = \left[\omega_{\text{m}}^2 - \omega(\omega + 2i\gamma)\right]p(\omega), \tag{26}$$

allows us to find $p(\omega)$ in terms of two ancillary functions, $E_{\text{m}}(\omega)$ and $\Delta\omega_{\text{m}}^2(\omega)$:

$$p(\omega) = \frac{q^2}{\mu}\frac{E_{\text{m}}(\omega)}{\omega_{\text{m}}^2 - \Delta\omega_{\text{m}}^2(\omega) - \omega(\omega + 2i\gamma)}. \tag{27}$$

The first of these ancillary functions,

$$E_{\text{m}}(\omega) = \sum_h eC_h I_h(\mathbf{x}, \omega)\left[\mathbf{u}_h^{\text{in}}(\mathbf{r}_{\text{m}}) - \alpha_h(\omega)\mathbf{u}_h^{\text{out}}(\mathbf{r}_{\text{m}})\right]\cdot\hat{\mathbf{n}}, \tag{28}$$

is the electric field along $\hat{\mathbf{n}}$ driving the molecular dipole (m). The $\mathbf{u}_h^{\text{in}}$ terms encode the field of the electron beam, and the $\mathbf{u}_h^{\text{out}}$ terms encode the nanoparticle's induced field. For our model parameters in Sec. V, at the adsorption site the induced

field from the nanoparticle will be much larger than the direct field from the electron beam.

The function in the denominator of $p(\omega)$,

$$\Delta\omega_{\rm m}^2(\omega) = \frac{q^2}{\mu}\sum_h C_h\alpha_h(\omega)\left|\mathbf{u}_h^{\rm out}(\mathbf{r}_{\rm m})\cdot\hat{\mathbf{n}}\right|^2, \tag{29}$$

arises from the electrostatic interaction of the dipole with its image charge, shifting the natural resonance $\omega_{\rm m}$ to a lower frequency. Physically, given a molecular dipole $p(\omega)\hat{\mathbf{n}}$ outside the dielectric particle surface, we would expect an additional field $\mathbf{E}_{\rm m}^{\rm m}(\mathbf{r}_{\rm m})\cdot\hat{\mathbf{n}}$ induced by the molecule in the particle to act back on the molecule along its dipole axis. This field is

$$\mathbf{E}_{\rm m}^{\rm m}\cdot\hat{\mathbf{n}} = -p(\omega)\Delta\omega_{\rm m}^2(\omega). \tag{30}$$

Hence the frequency shift is proportional to the electric field per unit dipole at the molecular site induced by the molecule itself, a sort of self-interaction.

C. The EEL spectrum

Now we can find the total potential $\Phi(\mathbf{r},\omega)$ that acts back on the beam electron. Given our solutions for $A_h(\omega)$ and $p(\omega)$, the only subtlety here is that we use the alternative dipole expansion, since the beam electron passes outside the molecule on the nanoparticle surface:

$$\Phi(\mathbf{r},\omega) = \Phi_{\rm m}^{\rm out}(\mathbf{r},\omega) + \sum_h A_h(\omega)\phi_h^{\rm out}(\mathbf{r}). \tag{31}$$

Next we find the work done on the beam electron by this potential, and by switching the integration order of ω and z, we extract the EEL spectrum [32]:

$$\frac{dP}{d\omega} = \frac{e}{\pi\hbar}{\rm Im}\left(\int_{-\infty}^{\infty}\frac{dz}{v}\Phi(\mathbf{r},\omega)e^{-i\omega z/v}\right). \tag{32}$$

We find that the EEL spectrum splits neatly into two parts, one that matches that of the bare nanoparticle (without the adsorbed molecule), and one that captures how the molecule alters the spectrum:

$$\underbrace{\frac{dP}{d\omega}}_{\text{full}} = \underbrace{\frac{dP_0}{d\omega}}_{\text{bare nanoparticle}} + \underbrace{\frac{dP_{\rm m}}{d\omega}}_{\text{molecule}}. \tag{33}$$

The bare nanoparticle spectrum takes on the form

$$\frac{dP_0}{d\omega} = \frac{e^2}{\pi\hbar}\sum_h C_h|I_h(\mathbf{x},\omega)|^2{\rm Im}[\alpha_h(\omega)]. \tag{34}$$

The molecular contribution to the spectrum depends on the dipole amplitude $p(\omega)$. It can be written as

$$\frac{dP_{\rm m}}{d\omega} = \frac{1}{\mu}\frac{q^2}{\pi\hbar}{\rm Im}\left(\frac{E_{\rm m}(\omega)E_{\rm e}(\omega)}{\omega_{\rm m}^2 - \Delta\omega_{\rm m}^2(\omega) - \omega(\omega+2i\gamma)}\right), \tag{35}$$

where $E_{\rm m}(\omega)$ and $\Delta\omega_{\rm m}^2(\omega)$ are given by Eqs. (28) and (29), respectively, and $E_{\rm e}(\omega)$ is given by a function similar to but distinct from $E_{\rm m}(\omega)$:

$$E_{\rm e}(\omega) = \sum_h eC_h\bar{I}_h(\mathbf{x},\omega)[\bar{\mathbf{u}}_h^{\rm in}(\mathbf{r}_{\rm m}) - \alpha_h(\omega)\bar{\mathbf{u}}_h^{\rm out}(\mathbf{r}_{\rm m})]\cdot\hat{\mathbf{n}}. \tag{36}$$

The function $E_{\rm e}(\omega)$ arises from the electric field that acts back on the passing electron (e), with the $\bar{\mathbf{u}}_h^{\rm in}$ terms encoding the direct field from the molecule, and the $\bar{\mathbf{u}}_h^{\rm out}$ terms encoding the field from the particle induced by the vibrating molecule. As with $E_{\rm m}(\omega)$, for our model parameters in Sec. V, the induced field tends to dominate the direct field.

Signal enhancement thus roughly takes the following route: the electron beam induces an electric field in the nanoparticle, which drives the molecular dipole, which induces a response electric field in the nanoparticle, which then acts back on the electron beam. Equation (35) will be analyzed further in Sec. V.

IV. NANOPARTICLE SHAPE EFFECTS

Before presenting our results for vibrational enhancement, we review here the EELS spectra obtained from bare nanoparticles with five canonical geometries (semi-infinite foil, semi-infinite circular cylinder, sphere, oblate spheroid, and prolate spheroid). This is useful for gaining an appreciation of how the frequencies plotted in Fig. 1 are manifest in the EEL spectra. The spectra for prolate spheroids, and the changes in these spectra as a result of shape eccentricity, will be especially relevant to the enhancement results presented in Section V.

The bare nanoparticle spectra in this section were computed by applying Eq. (34). We use experimentally measured parameters for cubic boron nitride [33], an isotropic material, but with an unrealistically small damping parameter ($\eta = 0.0005\omega_0$) to isolate the modes. For all plots going forward, we assume a 60 keV electron beam and a 1 mrad collection semi-angle.

A. Foil, cylinder, sphere

Figure 3 shows spectra for the three "limiting" geometries, namely, the foil, the cylinder, and the sphere (see Fig. 1). In each plot, three frequencies are marked: ω_0 as the lower bound for the harmonic frequencies, ω_ℓ as the upper bound, and a frequency between the two that picks out the intermediate value associated with $\epsilon_h = -1$ (which is the frequency associated with modes of high spatial frequency as $h\to\infty$; see Fig. 1).

For the foil [19], as a general rule the cosh modes scatter strongly, whereas the sinh modes do not. This behavior is easily understood from the projection integral along the beam direction in Eq. (32): the antisymmetry of the sinh potentials implies that their projection almost vanishes for foil thicknesses $\ll v/\omega$, which is the case here. For the thicker foil in Fig. 3, the peak around $\omega(\epsilon_h = -1)$ is due to a large density of states, although the states are individually very weakly scattering.

For the semi-infinite cylinder with its axis perpendicular to the electron beam [34], modes above $\omega(\epsilon_h = -1)$ are not present. The cylinder spectra depend on beam position. While the broad band extending down to ω_0 representing excitations of the $m = 0$ states can be seen in spectra both when the beam pierces the center of the cylinder and when the beam is aloof, the odd m bands are missing from the piercing beam spectrum, by symmetry.

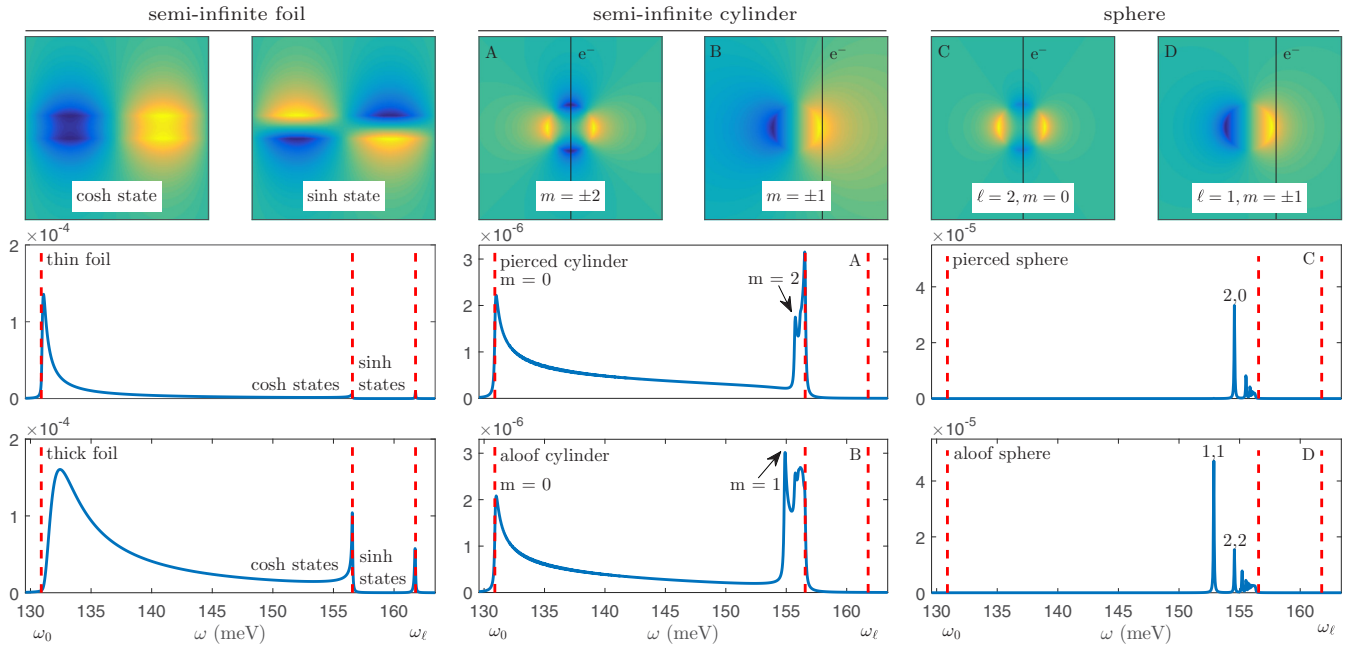

FIG. 3. Bare nanoparticle spectra for the three "limiting" geometries. Left: Thin (5 nm) and thick (50 nm) semi-infinite foil. Middle: Semi-infinite cylinder of diameter $2a = 50$ nm with (A) piercing beam at $b = 0$, and (B) aloof beam at $b = 1.01a$. Right: Sphere of diameter $2a = 50$ nm with (C) piercing beam at $b = 0$, and (D) aloof beam at $b = 1.01a$. Spectra are plotted in units of meV^{-1}. For each geometry, representative harmonic potentials are shown atop, with the electron beam trajectory indicated by a solid black line when relevant.

The solid harmonics for the sphere are in terms of the familiar spherical harmonics. As with the cylinder, the spectra for the sphere [32,35] are also a function of position—that is, the odd m states are again suppressed by symmetry for the centrally piercing beam. The sphere is highly degenerate, with $\omega_{\ell m}$ a function of ℓ alone, and its allowed range of harmonic frequencies is narrow, limiting shape effects.

B. Oblate and prolate spheroids

Figure 4 shows spectra for the two "intermediate" geometries, namely, the oblate spheroids (intermediate between sphere and foil), and the prolate spheroids (intermediate between sphere and cylinder). The Appendix includes details of the spheroidal coordinate systems and their solid harmonics. In Fig. 4, the spheroid spectra become redshifted and "spread out" with increasing cross-sectional eccentricity. For the oblate and prolate spheroids [36], shape effects become increasingly pronounced as the nanoparticle eccentricity e increases (when $e \to 0$, both recover the sphere). The oblate spheroidal harmonics stretch the sphere's harmonics into broad, flat regions at the poles, with even ℓ values mimicking cosh-type foil states at large e, and odd ℓ values mimicking sinh-type foil states. The prolate spheroidal harmonics (in our unconventional rendering) tip and stretch the sphere's $\vartheta = 0$ axis along the x axis, thus mimicking the azimuthal dependence of the cylindrical harmonics on m while retaining the discrete ℓ modes of the sphere in place of the semi-infinite cylinder's continuous ks.

The symmetries of the oblate spheroid are such that only b, the beam's transverse distance from the origin, is relevant to spectral differences. Comparing the spectra for $b = 0$ and $b = 1.01R$ in Fig. 4, where R is the projected spheroid radius, we find that the aloof beam excites a wider range of energies than the piercing beam, and that there are roughly twice as many peaks in the aloof beam spectra as the piercing beam spectra. Specifically, the states with $\ell = 2, 4, 6, \ldots$ and $m = 0$ are most excited by the piercing beam, and the states with $\ell = 1, 2, 3, \ldots$ and $m = \pm\ell$ are most excited by the aloof beam. In both cases, the preferentially excited states are locally coshlike, with a single type of coordinated surface charge near the STEM beam.

Beam position is even more important for prolate spheroid spectra. As with the oblate case in Fig. 4, for the prolate spheroids we position one beam at the center and one just outside the nanoparticle, past the tip at $(x, y) = (1.01R, 0)$. Again, the aloof beam excites roughly twice as many frequencies as the piercing beam, but for the prolate spheroid we observe the *same* excited frequencies for our two chosen beam positions, only with half of the peaks missing from the spectra of the piercing beam. Specifically, while the aloof beam strongly excites the states with $\ell = 1, 2, 3, \ldots$ and $m = 0$, the piercing beam only excites the states with $\ell = 2, 4, 6, \ldots$ and $m = 0$. Preferentially excited modes here are antennalike, but modes with an odd spatial parity are suppressed for the piercing beam, as with the sphere and cylinder.

V. MOLECULAR ADSORBATE SIGNALS

In this section, we present detailed simulations of the enhancement of the EELS signal from an adsorbed molecule on the surface of a prolate-spheroidal Drude-metal nanoparticle. In Fig. 4, we see that the mode frequencies of the prolate spheroids exhibit large redshifts with increasing eccentricity. For a Drude metal considered in this section, the behavior will be similar, but with stretched high- and low-frequency

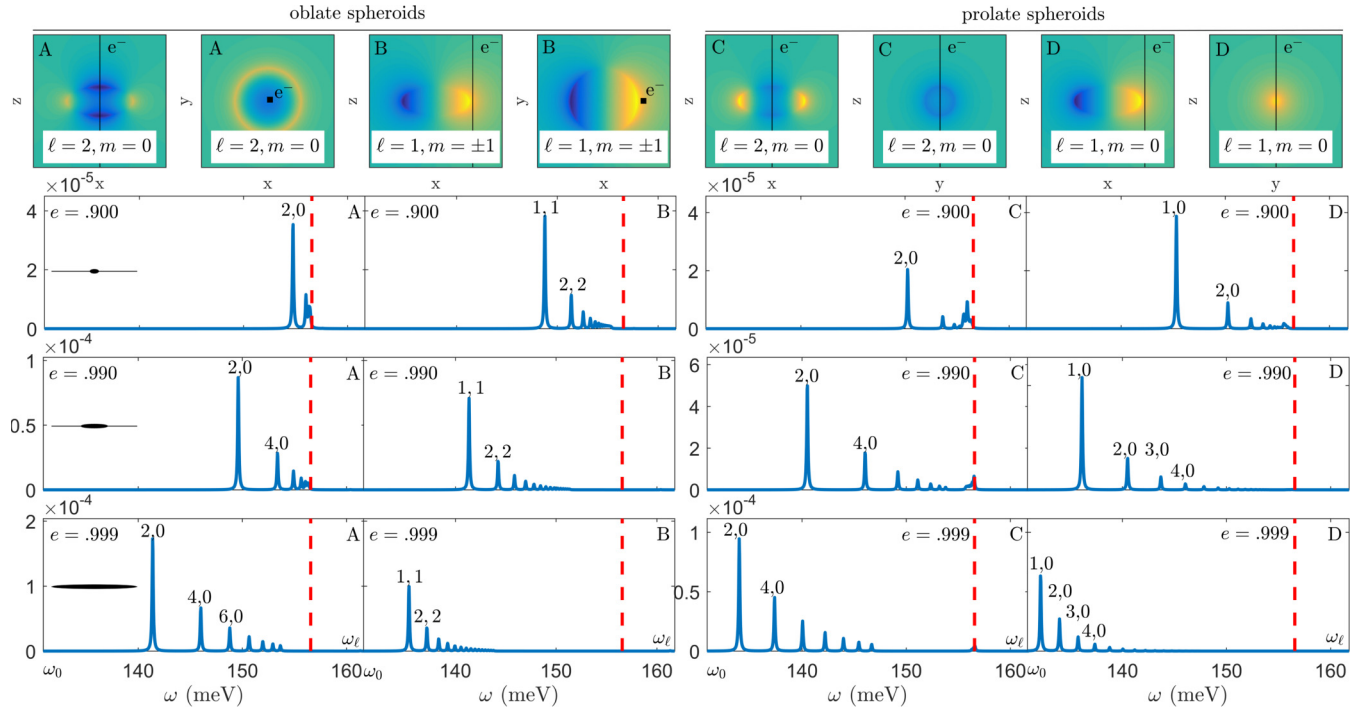

FIG. 4. Bare nanoparticle spectra for the two "intermediate" geometries. Oblate (left) and prolate (right) spheroids of maximal thickness $2a = 50$ nm over a wide range of eccentricity. In the oblate spheroid spectra, beam positions are (A) through the center $b = 0$, or (B) just past the edge R of the nanoparticle at $b = 1.01R$. In the spectra for prolate spheroids of length $2R$, beam positions are either (C) piercing their centers, both in length and width, or (D) aloof just past the lengthwise tip, at $(x_0, y_0) = (1.01R, 0)$. Spectra are plotted in units of meV^{-1}. Representative harmonic potentials in plan view and cross-section view are shown atop, with the electron beam trajectory indicated.

limits $\omega_\ell \to \omega_p/\sqrt{\epsilon_\infty}$ and $\omega_0 \to 0$. Thus the surface plasmonic excitations of prolate spheroidal metallic nanoparticle with large eccentricity are shifted into the infrared, and hence can be used to enhance molecular vibrations. In some cases, the nanoparticle excitations can be "tuned" to a resonance condition, giving a large degree of enhancement, as shown below. Generally, we expect that a molecule positioned at a higher curvature site on the nanoparticle surface will experience a larger electric field, and thus a larger degree of EELS enhancement. Hence we consider molecules adsorbed on the tips of prolate spheroids (our results for molecules on oblate spheroids follow similar trends but are not presented).

As before, we deploy a 60 keV beam, but now we assume it has a finite energy width described by a Gaussian distribution with a full-width at half-maximum (FWHM) of 5 meV. The nanoparticle's Drude parameters are taken to be those of silver [37]: $\hbar\omega_p = 8.9$ eV, $\hbar\eta = 0.10$ eV, $\epsilon_\infty = 5$. The molecule is defined via its charge q, reduced mass μ, resonant frequency ω_m, and damping parameter γ; we have used $q = e$, $\mu = 1$ amu, $\hbar\omega_m = 530$ meV, and $\hbar\gamma = 12$ meV. This large natural damping γ has been chosen to compensate for another omission in our calculations.

For an adsorbed molecule realistically near the nanoparticle surface, the predicted frequency shift from $\Delta\omega_m^2(\omega)$ [Eq. (29)] is unrealistically large. One reason for this overestimation is that a point dipole (representing the molecule in our model) can interact with the arbitrarily fine spatial variations of the arbitrarily high-order harmonic modes. However, a model similar to ours included finite-size effects [38] but also overestimated the frequency shifts observed in IR studies. To address this problem, we have set $\Delta\omega_m^2(\omega)$ to *zero* by fiat. But this breaks self-consistency, so we need to introduce a large γ to maintain positivity for all spectra. The effect of setting $\Delta\omega_m^2(\omega)$ to zero should be a systematic underestimate of the molecular signal (since signal is inversely related to frequency), and a systematic overestimate of the molecular signal-to-noise (since this neglects any additional particle-mediated peak broadening). The function $\Delta\omega_m^2(\omega)$ captures the interaction of the molecular dipole with its own image dipole, so its neglect also eliminates the ability of more sharply curved absorption sites to encourage larger molecular resonance redshifts.

A. Off- vs on-resonance—Fano line shapes

Since the molecular damping γ is small compared to the dielectric particle damping η, the phase of the molecular vibration varies quickly relative to phase of the nanoparticle's induced electric field. As shown below, when a resonance condition is approached, that is, when a nanoparticle mode frequency approaches the molecular frequency, we typically obtain a strong Fano-type asymmetric spectral signature [39] in the molecular spectrum $dP_m/d\omega$. If the molecular frequency is far separated from any of the nanoparticle's harmonic frequencies, then $dP_m/d\omega$ reverts to a weaker symmetric bump poking above the bare nanoparticle signal.

We introduce the dimensionless frequency variable $\Omega = (\omega - \omega_m')/\gamma'$. (The primes on these parameters reflect that they include contributions from the particle, downshifting the molecular resonance ω_m and broadening the damping γ.)

Near the molecular resonance, the fields $E_m(\omega)$ and $E_e(\omega)$ [Eqs. (28) and (36)] can be estimated, respectively, by $|E_m(\omega'_m)|\exp(i\theta_m)$ and $|E_e(\omega'_m)|\exp(i\theta_e)$. Substituting into Eq. (35) yields an approximate expression for the molecular contribution to the spectrum

$$\frac{dP_m}{d\omega} \approx \frac{1}{\mu}\frac{q^2}{\pi\hbar}\frac{|E_m(\omega'_m)E_e(\omega'_m)|}{2\omega'_m\gamma'}\left(\frac{\cos(\delta)-\Omega\sin(\delta)}{1+\Omega^2}\right), \quad (37)$$

where $\delta = \theta_m + \theta_e$. In Eq. (37) the values $\delta = 0$ and π correspond to positive- and negative-symmetric line shapes, respectively, whereas $\delta = \pi/2$ and $3\pi/2$ correspond to asymmetric line shapes. For our model parameters, the fields $E_m(\omega)$ and $E_e(\omega)$, and hence the phase δ, are dominated by the nanoparticle response.

Well below the nanoparticle frequencies (off-resonance), the nanoparticle responds "in phase" with the Fourier-decomposed field of the electron beam. Hence $\delta = 0+0=0$, corresponding to a positive-symmetric line shape. At a nanoparticle frequency ω_h (on-resonance), the phase of the response due to mode h is $\pi/2$. Thus, in a simple picture consisting of just the single nanoparticle mode h, at resonance $\delta = \pi/2+\pi/2=\pi$, corresponding to a negative-symmetric line shape. The molecular spectrum $dP_m/d\omega$ sits atop the bare nanoparticle spectrum $dP_0/d\omega$, so the condition that $dP_m/d\omega < 0$ implies that the field causing the beam electron's energy loss is weaker in the presence of the molecule.

With the nanoparticle modes at other frequencies included, we observe that δ can deviate significantly from the "simple resonance value" π. Hence, at a resonance condition, we can obtain Fano-type line shapes with significant asymmetry, with the asymmetry arising ultimately from multimodal contributions.

Figure 5 compares line shapes for the molecule adsorbed on the surface of a sphere and a prolate spheroid. The sphere, with its low eccentricity, gives an off-resonance condition with $\delta \approx 0$, leading to a symmetric line shape. At the resonance condition $\omega_m \approx \omega_{10}$ (i.e., the molecular frequency matches the harmonic frequency associated with $\ell = 1$, $m = 0$), the phase $\delta \approx \pi/4$ ($\neq \pi$ due to multimodal contributions), leading to a Fano-type asymmetric line shape. These spectral features are similar to those predicted in the recent work of Konečná *et al.* [23] who modeled the spectral response of thin dielectric layers, representing molecular layers, on nanoparticle surfaces.

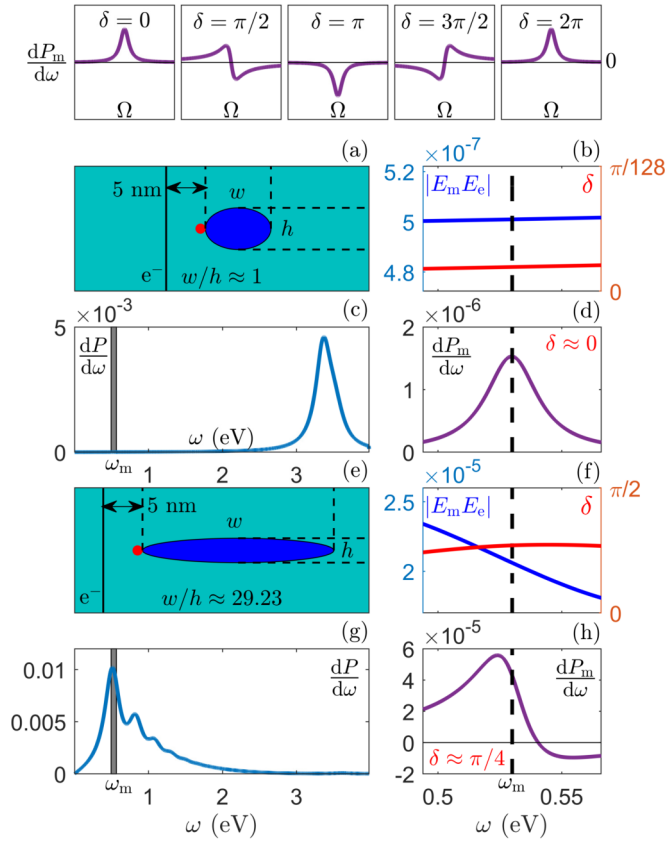

FIG. 5. Relating enhanced molecular line shapes to δ, the cumulative phase shift from E_m and E_e (top row). In (a)–(d) the molecule adsorbed on a silver sphere gives an off-resonance condition (c) leading to $\delta \approx 0$ and hence a symmetric line shape (d). In (e)–(h), a long prolate spheroid gives an on-resonance condition (g) leading to $\delta \approx \pi/4$ and hence an asymmetric line shape (h). The grey strips in (c) and (g) indicate the plotting range used in (b), (d), (f), and (h). The red dot indicates the molecule (the cartoons are not to scale). The sphere and spheroid both have a central thickness $h = 50$ nm.

B. Quantifying signal enhancement

The intensity of the enhanced molecular signal is most easily characterized in the off-resonance limit that $\delta = 0$ and the line shape is symmetric. Analytically, if we assume that the electric field $\mathbf{E}^{\text{out}}(\mathbf{r}_m, \omega)$ varies slowly in ω near the bare molecular frequency ω'_m, and that the molecular damping factor $\gamma' \ll \omega'_m$, the total integrated enhanced signal is

$$P_m \approx \frac{q^2}{2\hbar\omega'_m\mu}|\mathbf{E}^{\text{out}}(\mathbf{r}_m, \omega'_m)\cdot\hat{\mathbf{n}}|^2, \quad (38)$$

where, as before, γ' and ω'_m are the shifted parameters. This is the same as for a bare molecule, except the field $|\mathbf{E}^{\text{out}}(\mathbf{r}_m, \omega'_m)\cdot\hat{\mathbf{n}}|^2$ now contains contributions from the dielectric, and not only the beam electron.

Hence the enhanced signal is proportional to the square of the field at the molecular site. Intuitively, this is squared because one factor of the electric field arises from the molecular excitation, and one factor arises from the molecule acting back on the nanoparticle. This contrasts with the case of surface-enhanced Raman spectroscopy, in which the signal enhancement scales roughly as the electric field enhancement to the fourth power: two powers for photoabsorption, and two for photoemission [40].

Figure 6 illustrates how we have quantified the signal, using the same physical situations as in Fig. 5. The full EEL spectrum $dP/d\omega$ (plotted in blue) is dominated by the nanoparticle, but the presence of the molecule causes the spectrum to depart from the bare nanoparticle spectrum $dP_0/d\omega$. This departure constitutes the enhanced molecular spectrum $dP_m/d\omega$ (plotted in purple). Compared to the bare molecular spectrum $dP^0_m/d\omega$ (plotted in red), for which the nanoparticle is absent, the enhanced molecular spectrum exhibits greater intensity, since the adsorbed molecule is coupled to the nanoparticle.

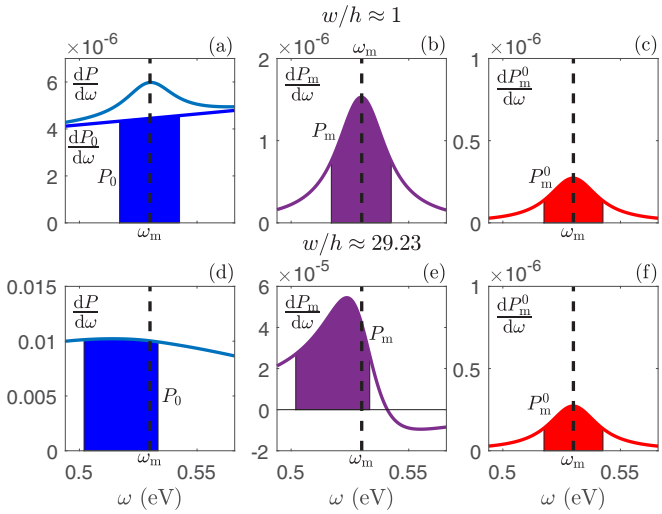

FIG. 6. Quantifying signal enhancement. Plots (a)–(c) show signals for the sphere of Fig. 5, and plots (d)–(f) show signals for the prolate spheroid of Fig. 5. The molecular signal P_{m} in (b) and (e) is estimated by finding the maximal feature in the enhanced spectrum and integrating the FWHM. The bare-nanoparticle signal P_0 in (a) and (d) is found by integrating the same spectral region for the background. The bare molecular signal P_{m}^0 in (c) and (f) is equal for both cases, as it only depends on the beam distance from the molecule (5 nm throughout).

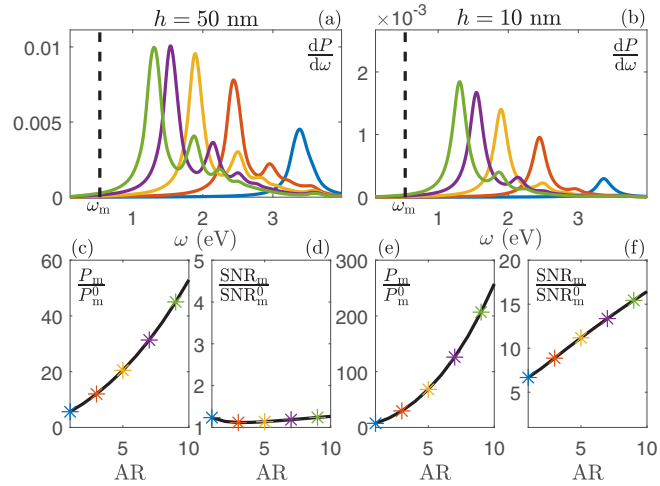

FIG. 7. (a), (b) Full EEL spectra;(c), (e) signal enhancements; (d), (f) and SNR enhancements for adsorbed moleules on the tip of prolate spheroids of aspect ratios (AR $= w/h$) between 1 and 10 (specific ARs are color coded). Cases of constant thickness are shown, both with $h = 50$ nm (left) $h = 10$ nm (right).

Figure 6 defines three quantities: the background signal from the nanoparticle P_0, the enhanced molecular signal P_{m}, and the bare molecular signal P_{m}^0. We then define

$$\text{signal enhancement} = \frac{P_{\mathrm{m}}}{P_{\mathrm{m}}^0}. \tag{39}$$

The signal enhancement is defined relative to the bare molecular signal. The widths of the peaks in $dP_{\mathrm{m}}/d\omega$ and $dP_{\mathrm{m}}^0/d\omega$ are determined both by the particle damping γ and the beam's energy width. For each, we integrate over the FWHM so that the signal enhancement is insensitive to the beam's energy width.

The enhanced molecular spectrum sits atop the spectrum from the nanoparticle, so we also quantify the enhancement of the signal-to-noise ratio (SNR) of the molecular signal, assuming Poisson noise only:

$$\text{SNR enhancement} = \frac{\mathrm{SNR}_{\mathrm{m}}}{\mathrm{SNR}_{\mathrm{m}}^0} \approx \frac{P_{\mathrm{m}}/\sqrt{P_0}}{P_{\mathrm{m}}^0/\sqrt{P_{\mathrm{m}}^0}} = \frac{P_{\mathrm{m}}}{\sqrt{P_0 P_{\mathrm{m}}^0}}. \tag{40}$$

The SNR enhancement is defined relative to the $\mathrm{SNR}_{\mathrm{m}}^0$ of the bare molecular signal. The SNR enhancement depends on the background signal P_0 which is proportional to the integration interval, scaling inversely with the square root of the molecular peak width.

C. Off-resonance enhancement

Figure 7 shows how the signal enhancement and the SNR enhancement vary as the prolate spheroid's aspect ratio (AR = width/height) changes from 1 to 10. Both "thick" ($h = 50$ nm) and "thin" ($h = 10$ nm) prolate spheroids are considered. All these are off-resonance cases where the nanoparticle mode frequencies lie well above the molecule's frequency ω_{m}. For AR $= 10$, we find the greatest signal enhancements of about 50 in the thick case, versus about 250 in the thin case. The greater enhancement for the thin nanoparticles comes from the sharper tip, and hence the stronger fields at the adsorption site. The results here also give us our first confirmation that small, sharp nanoparticles will help the most with signal enhancement. Along with its sharper tip, a small nanoparticle contributes a lesser background signal, allowing the molecular signal to stand out. For AR $= 10$, our calculations in Fig. 7 predict a SNR enhancement barely above unity for the thick nanoparticle, versus about 16 for the thin nanoparticle.

In Fig. 8, we explore how the SNR enhancement varies more generally. First consider the red curves, which use the same nanoparticle/beam geometry as above. For a fixed nanoparticle thickness $h = 10$ nm, we investigate how the molecular signal, the signal enhancement, and the SNR enhancement vary with nanoparticle length, specified by w, keeping the beam distance from the adsorbate constant at 5 nm. The signal enhancement increases with increasing nanoparticle length, which is readily understood in terms of the local electric field, as explained above. In the colormap figures, we notice that the SNR enhancement is more closely aligned with the thickness h of the nanoparticle than with the aspect ratio.

The blue and grey curves in Fig. 8 investigate another possibility, as raised by Konečná *et al.* [23]. They reported the possibility of "ultraremote sensing," with the beam on the opposite side of the nanoparticle as the adsorbate, as shown in our cartoon by beam B. While the model of Konečná *et al.* differs from ours—they use a thin dielectric layer on the nanoparticle surface rather than a point dipole—our results are consistent. At far beam distances, the intrinsically small signal from the bare molecule allows for enormous signal and SNR enhancements. But when the "ultraremote enhancement" is defined in terms of the expected signal for case A, as in the

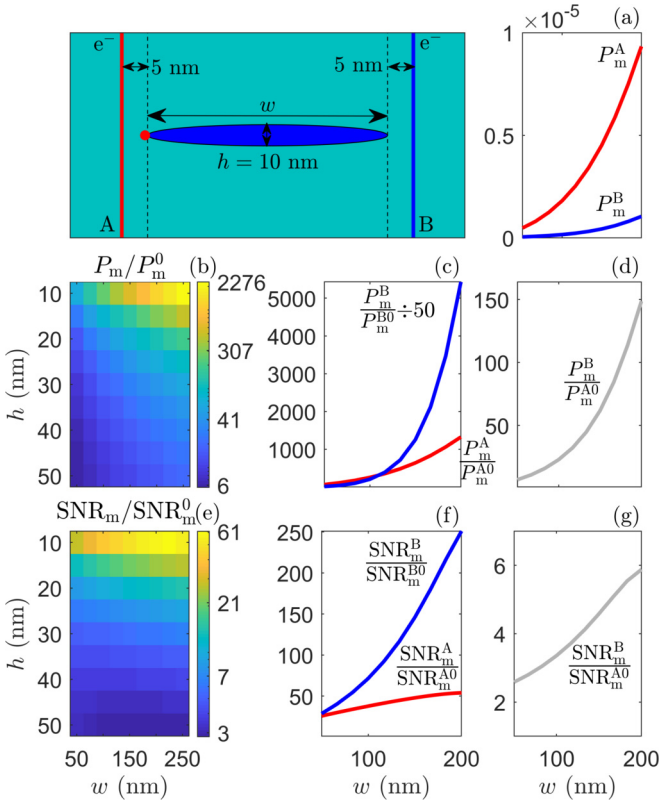

FIG. 8. Results are given for beam positions adjacent to the molecule (A) and opposite to the molecule (B), with the beam 5 nm from the particle in each case. The colormap plots (b) and (e) summarize many different cases for the adjacent beam (A). Plots (a), (c), and (f) contrast outcomes from beams A and B in terms of the definitions given in the main text, while (d) and (g) compare the results of beam B to the benchmarks used for beam A.

grey curves in Fig. 8, we find smaller relative enhancements for the ultraremote beam B that one might expect.

D. On-resonance enhancement

Pushing toward higher aspect ratios, Fig. 9 shows how particle resonances can be harnessed to improve enhancements further still. An obvious possibility is to tune the aspect ratio of the particle such that the lowest particle resonance ω_{10} (that is, the resonance corresponding to mode $\ell = 1, m = 0$) aligns with the molecular resonance ω_{m}. This leads to enormous signal enhancements, up to several thousand times, with the signal manifesting as a Fano-type dip into rather than a bump atop the nanoparticle background. But such dips are sensitive to the beam energy resolution, and the position of the dip atop a particle resonance limits the achievable SNR enhancement.

One way both to lower the nanoparticle background signal and to regain an asymmetric bump in place of the resonant dip is to tune the particle resonance ω_{10} such that it lies just above the molecular resonance $\omega_{\mathrm{m}} - 2\eta$ above, say, such that the molecular resonance lies on the bottom edge of the particle resonance. Figure 9 shows that such particles will produce roughly half the signal enhancement of the particles tuned to overlap the molecular resonance directly, yet such off-resonant tuning is able to achieve somewhat better SNR

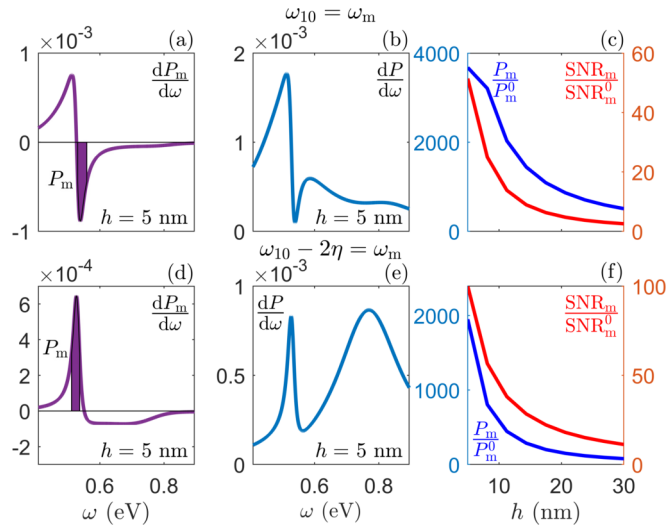

FIG. 9. Calculations for adsorbates on prolate spheroids with fixed AR = 29.23 [(a)–(c), with ω_{10} matching ω_{m}], and AR = 18.32 [(d)–(f), with $\omega_{10} - 2\eta$ matching ω_{m}]. For thickness $h = 5$ nm, (a) and (d) show the molecular spectra, while (b) and (e) show the total spectra. In (c) and (f), we quantify the signal enhancement (in blue) and the SNR enhancement (in red) for the two cases.

enhancements, with the SNR enhancement approaching 100 for small particles of $h = 5$ nm.

VI. CONCLUSIONS

We applied the Born-Huang phenomenological theory in the electrostatic approximation to model the optical vibrations in finite dielectric nanoparticles. We reviewed the qualitative features of the electron energy-loss (EEL) spectra obtained in the STEM for five canonical nanoparticle geometries (foil, oblate spheroid, sphere, prolate spheroid, and cylinder). We reviewed how the associated solid harmonics for these geometries allow us calculate the resonant frequencies of the various modes. We also emphasized the applicability of the same theory, with a suitably altered dielectric function, to describe surface plasmon excitations in finite metallic nanoparticles.

We then showed how the Born-Huang theory can be extended to model the enhancement of the vibrational EEL signal from a molecule, regarded as a point dipole, adsorbed on the surface of a metallic nanoparticle. The degree of enhancement was found to be proportional to the square of the local electric field at the adsorption site. Detailed expressions for the associated energy-loss spectrum were derived. These expressions for the spectrum split neatly in two parts, one from the bare nanoparticle, and the other from the molecule.

We predicted the degree of enhancement of the vibrational STEM-EELS signal for a molecular dipole adsorbed on the tip of a prolate spheroidal metallic nanoparticle having the dielectric properties of silver. For the parameters stated in the main text, our calculations indicate that signal enhancements of several hundred times are readily achieved for nanoparticles of suitably small thickness (e.g., 10 nm) and high aspect ratio (e.g., 10). The enhancement is maximized by the larger electric fields associated with a sharper nanoparticle tip. Tuning the nanoparticle surface plasmon frequency to the molecular

TABLE I. Convenient coordinates. Contra tradition; here the cylinder and prolate spheroid lie along x rather than z.

Geometry	Coordinates, ξ_i	Coordinate ranges	Scale factors, h_i
foil	$x = \xi_2$	$-\infty < \xi_1 < \infty$	$h_1 = 1$
	$y = \xi_3$	$-\infty < \xi_2 < \infty$	$h_2 = 1$
	$z = \xi_1$	$-\infty < \xi_3 < \infty$	$h_3 = 1$
circular cylinder	$x = \xi_3$	$0 \leqslant \xi_1 < \infty$	$h_1 = 1$
	$y = \xi_1 \cos(\xi_2)$	$0 \leqslant \xi_2 < 2\pi$	$h_2 = \xi_1$
	$z = \xi_1 \sin(\xi_2)$	$-\infty < \xi_3 < \infty$	$h_3 = 1$
sphere	$x = \xi_1 \sin(\xi_2)\cos(\xi_3)$	$0 \leqslant \xi_1 < \infty$	$h_1 = 1$
	$y = \xi_1 \sin(\xi_2)\sin(\xi_3)$	$0 \leqslant \xi_2 \leqslant \pi$	$h_2 = \xi_1$
	$z = \xi_1 \cos(\xi_2)$	$0 \leqslant \xi_3 < 2\pi$	$h_3 = \xi_1 \sin(\xi_2)$
oblate spheroid	$x = c[(1+\xi_1^2)(1-\xi_2^2)]^{1/2}\cos(\xi_3)$	$0 \leqslant \xi_1 < \infty$	$h_1 = c[(\xi_1^2+\xi_2^2)/(\xi_1^2+1)]^{1/2}$
	$y = c[(1+\xi_1^2)(1-\xi_2^2)]^{1/2}\sin(\xi_3)$	$-1 \leqslant \xi_2 \leqslant 1$	$h_2 = c[(\xi_1^2+\xi_2^2)/(1-\xi_2^2)]^{1/2}$
	$z = c\,\xi_1\xi_2$	$0 \leqslant \xi_3 < 2\pi$	$h_3 = c[(\xi_1^2+1)(1-\xi_2^2)]^{1/2}$
prolate spheroid	$x = c\,\xi_1\xi_2$	$1 \leqslant \xi_1 < \infty$	$h_1 = c[(\xi_1^2-\xi_2^2)/(\xi_1^2-1)]^{1/2}$
	$y = c[(\xi_1^2-1)(1-\xi_2^2)]^{1/2}\cos(\xi_3)$	$-1 \leqslant \xi_2 \leqslant 1$	$h_2 = c[(\xi_1^2-\xi_2^2)/(1-\xi_2^2)]^{1/2}$
	$z = c[(\xi_1^2-1)(1-\xi_2^2)]^{1/2}\sin(\xi_3)$	$0 \leqslant \xi_3 < 2\pi$	$h_3 = c[(\xi_1^2-1)(1-\xi_2^2)]^{1/2}$

frequency, signal enhancements of several thousand times are predicted by the model, with the spectral line shapes typically exhibiting significant Fano-type asymmetry due ultimately to multimodal contributions.

In summary, the present paper indicates that significant enhancements of molecular vibrational EELS signals can be achieved by coupling the vibrations of adsorbates to the plasmonic excitations of metallic nanoparticles. Such an effect could significantly increase the sensitivity of molecular vibrational STEM-EELS and, when combined with the simultaneous imaging capabilities of the STEM, could therefore provide a powerful tool for the characterization of surface-functionalized nanoparticles and nanomaterials for chemical sensing applications.

APPENDIX: GEOMETRIES AND COORDINATES

The five geometries treated in this paper correspond to respective coordinate systems for which Laplace's equation can be solved most easily via separation of variables [31,41]. For a more general approach, these could all be considered as versions of the confocal elliptic coordinate system with special symmetries.

In Table I, we summarize the coordinates we have used, including explicit scale factors for each system,

$$h_i = \sqrt{\left(\frac{\partial x}{\partial \xi_i}\right)^2 + \left(\frac{\partial y}{\partial \xi_i}\right)^2 + \left(\frac{\partial z}{\partial \xi_i}\right)^2}, \tag{A1}$$

which help us to find the gradient

$$\boldsymbol{\nabla} = \frac{\hat{\boldsymbol{\xi}}_1}{h_1}\frac{\partial}{\partial \xi_1} + \frac{\hat{\boldsymbol{\xi}}_2}{h_2}\frac{\partial}{\partial \xi_2} + \frac{\hat{\boldsymbol{\xi}}_3}{h_3}\frac{\partial}{\partial \xi_3}, \tag{A2}$$

the differential volume element

$$dV = h_1 h_2 h_3 d\xi_1 d\xi_2 d\xi_3, \tag{A3}$$

and the differential surface element

$$d\mathbf{S} = h_2 h_3 d\xi_2 d\xi_3 \hat{\boldsymbol{\xi}}_1, \tag{A4}$$

where we assume the surface is constant in ξ_1.

In Tables II and III, we give the harmonic functions for the five geometries. For the strictly finite geometries, we provide the Coulomb expansion coefficients of Eq. (16). For the spheroidal harmonics, Hobson [42] is an authoritative reference. To compute the associated Legendre functions of the second kind $Q_\ell^m(x)$ for $x > 1$, we used the method of Gil and Segura [43]. The projection integrals [Eq. (19)] are

TABLE II. Modes and potentials for the semi-infinite nanoparticle geometries, with spatial periods in infinite directions fixed by lengths L. Potentials need fixing to ensure continuity at particle boundaries.

Geometry	Mode labels, h	Inner potentials, ϕ_h^{in}	Outer potentials, ϕ_h^{out}
foil	$k_2 = 2\pi m/L_2$	$\phi_c = \cosh(\lvert\mathbf{k}\rvert\xi_1)\exp(i\mathbf{k}\cdot\boldsymbol{\xi})$	$\phi_{+z} = \exp(-\lvert\mathbf{k}\rvert\xi_1)\exp(i\mathbf{k}\cdot\boldsymbol{\xi})$
	$k_3 = 2\pi n/L_3$	$\phi_s = \sinh(\lvert\mathbf{k}\rvert\xi_1)\exp(i\mathbf{k}\cdot\boldsymbol{\xi})$	$\phi_{-z} = \exp(+\lvert\mathbf{k}\rvert\xi_1)\exp(i\mathbf{k}\cdot\boldsymbol{\xi})$
	$m, n = \pm1, \pm2, \pm3\ldots$	$\mathbf{k} = (k_2, k_3), \quad \boldsymbol{\xi} = (\xi_2, \xi_3)$	$\mathbf{k} = (k_2, k_3), \quad \boldsymbol{\xi} = (\xi_2, \xi_3)$
circular cylinder	$m = 0, \pm1, \pm2\ldots$	$I_M(\lvert k\rvert\xi_1)\exp(i(m\xi_2 + k\xi_3))$	$K_M(\lvert k\rvert\xi_1)\exp(i(m\xi_2 + k\xi_3))$
	$k = 2\pi n/L$		
	$n = \pm1, \pm2, \pm3\ldots$		

TABLE III. Potentials for the strictly finite nanoparticles with boundary ξ_1^0 [see Eq. (15)]. For these potentials, $\ell = 0, 1, 2\ldots$ and $m = -\ell\ldots+\ell$. Throughout, we use the notation $M = |m|$.

Geometry	$R_h^{\text{in}}(\xi_1)$	$R_h^{\text{out}}(\xi_1)$	$S_h(\xi_2,\xi_3)$	C_h
sphere	$\left(\frac{\xi_1}{\xi_1^0}\right)^\ell$	$\left(\frac{\xi_1^0}{\xi_1}\right)^{\ell+1}$	$P_\ell^M[\cos(\xi_2)]\exp(im\xi_3)$	$\frac{1}{\xi_1^0}\frac{(\ell-M)!}{(\ell+M)!}$
oblate spheroid	$P_\ell^M(i\xi_1)$	$\frac{Q_\ell^M(i\xi_1)}{P_\ell^M(i\xi_1^0)}$	$P_\ell^M(\xi_2)\exp(im\xi_3)$	$(2\ell+1)\frac{i(-1)^M}{c}\left(\frac{(\ell-M)!}{(\ell+M)!}\right)^2 P_\ell^M(i\xi_1^0)$
prolate spheroid	$P_\ell^M(\xi_1)$	$\frac{Q_\ell^M(\xi_1)}{P_\ell^M(\xi_1^0)}$	$P_\ell^M(\xi_2)\exp(im\xi_3)$	$(2\ell+1)\frac{(-1)^M}{c}\left(\frac{(\ell-M)!}{(\ell+M)!}\right)^2 P_\ell^M(\xi_1^0)$

the biggest remaining difficulty. Analytic solutions for these integrals are known for the sphere [32] and for the spheroids [36] when the projection is along the axis of rotational symmetry. For prolate spheroids oriented in the transverse plane, a different approach was needed. We were able to express the external prolate spheroidal harmonics via a convolution with the solid harmonics of the sphere, and by combining this with the rotated spherical solid harmonics [44], we constructed the projected prolate spheroidal potentials.

Although these methods are convenient mainly for "separable geometries," they are not limited to such geometries in principle. Consider a nanoparticle of a general shape whose harmonic potentials are determined using Eq. (13). Assuming that these harmonic potentials can be orthogonalized with respect to the nanoparticle surface, this enables a Coulomb expansion in terms of the potentials, as in Eq. (14). Using Green's identities, it can be shown that the expansion coefficients C_h are given by

$$C_h = 4\pi\left[\int d\mathbf{S}\cdot\left(\bar{\mathbf{u}}_h^{\text{out}}\phi_h^{\text{in}} - \mathbf{u}_h^{\text{in}}\bar{\phi}_h^{\text{out}}\right)\right]^{-1}. \tag{A5}$$

This form reduces to Eq. (16) when the radial and angular parts of the harmonic functions are separable.

[1] O. L. Krivanek, T. C. Lovejoy, N. Dellby, T. Aoki, R. W. Carpenter, P. Rez, E. Soignard, J. Zhu, P. E. Batson, M. Lagos, R. F. Egerton, and P. A. Crozier, Nature **514**, 209 (2014).
[2] T. Miyata, M. Fukuyama, A. Hibara, E. Okunishi, M. Mukai, and T. Mizoguchi, Microscopy **63**, 377 (2014).
[3] R. Nicholls, F. S. Hage, J. Yates, D. McCulloch, D. M. Kepaptsoglou, T. C. Lovejoy, N. Dellby, O. L. Krivanek, K. Refson, and Q. Ramasse, Microsc. Microanal. **21 (Suppl. 3)**, 1469 (2015).
[4] C. Dwyer, T. Aoki, P. Rez, S. L. Y. Chang, T. C. Lovejoy, and O. L. Krivanek, Phys. Rev. Lett. **117**, 256101 (2016).
[5] P. Rez, T. Aoki, K. March, D. Gur, O. L. Krivanek, N. Dellby, T. C. Lovejoy, S. G. Wolf, and H. Cohen, Nat. Commun. **7**, 10945 (2016).
[6] M. J. Lagos, A. Trügler, U. Hohenester, and P. E. Batson, Nature **543**, 529 (2017).
[7] P. Rez, Microsc. Microanal. **20**, 671 (2014).
[8] C. Dwyer, Phys. Rev. B **89**, 054103 (2014).
[9] J. R. M. Saavedra and F. J. Garcia de Abajo, Phys. Rev. B **92**, 115449 (2015).
[10] A. A. Govyadinov, A. Konečná, A. Chuvilin, S. Velez, I. Dolado, A. Y. Nikitin, S. Lopatin, F. Casanova, L. E. Hueso, J. Aizpurua, and R. Hillenbrand, Nat. Commun. **8**, 95 (2017).
[11] K. Venkatraman, P. Rez, K. March, and P. A. Crozier, Microscopy **67**, 14 (2018).
[12] C. Dwyer, Phys. Rev. B **96**, 224102 (2017).
[13] R. Englman and R. Ruppin, Phys. Rev. Lett. **16**, 898 (1966).
[14] R. Fuchs and K. L. Kliewer, Phys. Rev. **140**, A2076 (1965).
[15] R. Fuchs, K. L. Kliewer, and W. J. Pardee, Phys. Rev. **150**, 589 (1966).
[16] K. L. Kliewer and R. Fuchs, Phys. Rev. **144**, 495 (1966).
[17] K. L. Kliewer and R. Fuchs, Phys. Rev. **150**, 573 (1966).
[18] R. Fuchs and K. L. Kliewer, J. Opt. Soc. Am. **58**, 319 (1968).
[19] A. A. Lucas and E. Kartheuser, Phys. Rev. B **1**, 3588 (1970).
[20] A. A. Lucas, E. Kartheuser, and R. G. Badro, Phys. Rev. B **2**, 2488 (1970).
[21] P. Verma, Chem. Rev. **117**, 6447 (2017).
[22] P. G. Etchegoin and E. C. Le Ru, Basic electromagnetic theory of SERS, *Surface Enhanced Raman Spectroscopy* (Wiley-VCH, Weinheim, Germany, 2010), Chap. 1, pp. 1–37.
[23] A. Konečná, T. Neuman, J. Aizpurua, and R. Hillenbrand, ACS Nano **12**, 4775 (2018).
[24] M. Born and K. Huang, *Dynamical Theory of Crystal Lattices* (Oxford University Press, London, 1954).
[25] O. Madelung, *Introduction to Solid State Theory* (Springer-Verlag, Berlin, 1978).
[26] T. J. Davis and D. E. Gómez, Rev. Mod. Phys. **89**, 011003 (2017).
[27] J. Van Bladel, Midwestern Universities Research Association, Report No. 440 (1958).
[28] A. Lucas and M. Sunjic, Prog. Surf. Sci. **2**, 75 (1972).
[29] H. Lourenço-Martins and M. Kociak, Phys. Rev. X **7**, 041059 (2017).
[30] I. D. Mayergoyz, D. R. Fredkin, and Z. Zhang, Phys. Rev. B **72**, 155412 (2005).
[31] W. Smythe, *Static and Dynamic Electricity*, 2nd ed. (McGraw-Hill, New York,1950) .
[32] T. L. Ferrell, R. J. Warmack, V. E. Anderson, and P. M. Echenique, Phys. Rev. B **35**, 7365 (1987).
[33] M. I. Eremets, M. Gauthier, A. Polian, J. C. Chervin, J. M. Besson, G. A. Dubitskii, and Y. Y. Semenova, Phys. Rev. B **52**, 8854 (1995).

[34] N. Zabala, E. Ogando, A. Rivacoba, and F. J. García de Abajo, Phys. Rev. B **64**, 205410 (2001).
[35] M. Schmeits, J. Phys. C **14**, 1203 (1981).
[36] B. L. Illman, V. E. Anderson, R. J. Warmack, and T. L. Ferrell, Phys. Rev. B **38**, 3045 (1988).
[37] H. U. Yang, J. D'Archangel, M. L. Sundheimer, E. Tucker, G. D. Boreman, and M. B. Raschke, Phys. Rev. B **91**, 235137 (2015).
[38] G. Ford and W. Weber, Surf. Sci. **129**, 123 (1983).
[39] M. F. Limonov, M. V. Rybin, A. N. Poddubny, and Y. S. Kivshar, Nat. Photon. **11**, 543 (2017).
[40] E. L. Ru and P. Etchegoin, Chem. Phys. Lett. **423**, 63 (2006).
[41] L. Landau and E. Lifshitz, *Electrodynamics of Continuous Media* (Pergamon Press, Oxford, 1960).
[42] E. Hobson, *The Theory of Spherical and Ellipsoidal Harmonics* (Cambridge University Press, Cambridge, 1931).
[43] A. Gil and J. Segura, Comput. Phys. Commun. **108**, 267 (1998).
[44] N. A. Gumerov and R. Duraiswami, Recursive computation of spherical harmonic rotation coefficients of large degree, in *Excursions in Harmonic Analysis, Volume 3: The February Fourier Talks at the Norbert Wiener Center*, edited by R. Balan, M. J. Begué, J. J. Benedetto, W. Czaja, and K. A. Okoudjou (Springer International Publishing, Basel, 2015), pp. 105–141.